Microelectronic Engineering 274 (2023) 111967

Contents lists available at ScienceDirect

Microelectronic Engineering

journal homepage: www.elsevier.com/locate/mee

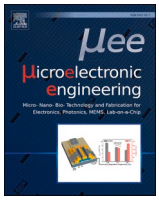

Micrometer-size crystalline monolayer MoS_2 domains obtained by sulfurization of molybdenum oxide ultrathin films

S.E. Panasci [a], E. Schilirò [a], A. Koos [b], M. Nemeth [b], M. Cannas [c], S. Agnello [a,c,d], F. Roccaforte [a], B. Pécz [b], F. Giannazzo [a,*]

[a] Consiglio Nazionale delle Ricerche - Istituto per la Microelettronica e Microsistemi (CNR-IMM), Strada VIII 5, 95121 Catania, Italy
[b] Centre for Energy Research, Institute of Technical Physics and Materials Science, Konkoly-Thege ut 29-33, 1121 Budapest, Hungary
[c] Department of Physics and Chemistry Emilio Segrè, University of Palermo, Via Archirafi 36, 90123 Palermo, Italy
[d] ATEN Center, University of Palermo, Viale delle Scienze Ed. 18, 90128 Palermo, Italy

ARTICLE INFO

Keywords:
MoS_2
Sulfurization
Transmission electron microscopy
Raman spectroscopy
Photoluminescence

ABSTRACT

In this work, the formation of micrometer-size crystalline monolayer (1L) MoS_2 flakes with triangular shape and a central multilayer core is obtained by the sulfurization at 800 °C of pre-deposited ultrathin MoO_x films (1.2–1.8 nm) on c-sapphire substrates. The thickness uniformity, crystalline quality, doping and strain distribution in the MoS_2 flakes as a function of the initial MoO_x thickness was evaluated by micro-Raman (μR) mapping. The excellent crystalline quality of the triangular 1L-MoS_2 flakes was confirmed by micro-photoluminescence (μPL) maps, showing a very intense peak at ~1.85 eV, that decreases in the central part, as expected for multilayers MoS_2. A biaxial strain of ~0.38–0.4% was deduced from the μPL data, in perfect agreement with μR results. Our results show how the sulfurization of pre-deposited MoO_x films on c-sapphire allows, under proper conditions, to obtain 1L-MoS_2 flakes with quality comparable to the one typically reported by the conventional chemical vapour deposition, with important implications for device applications.

1. Introduction

Molybdenum disulfide (MoS_2) is the most investigated two-dimensional (2D) material of the transition metal dichalcogenides (TMDs) family, thanks to its abundance in nature and the high chemical/mechanical stability in ambient conditions. In particular, the 2H-MoS_2 phase is characterized by semiconducting electrical properties, with a peculiar tunability of the bandgap as a function of the thickness, from an indirect bandgap (1.2 eV) in the bulk form to a direct bandgap (1.8–1.9 eV) for monolayer (1L) MoS_2 [1,2]. Such bandgap values in the visible - near infrared range are very interesting for a wide range of applications in different fields, including electronics [3], optoelectronics [4], photocatalysis [5] and sensing [6]. In particular, both 1L and multilayer MoS_2 have been employed as a channel material for field-effect transistors [7] with a high on/off ratio (10^8) [7,8] and good mobility (200–400 cm^2/Vs) [7,8], making them attractive to replace Si for the next generation ultra-scaled CMOS devices [9]. The production of large-area MoS_2 with control in term of thickness and crystal quality represents the main requirement for future applications. Currently, several top-down approaches, like micro-mechanical exfoliation [10,11], gold-assisted exfoliation [12–14], and liquid exfoliation [15], are employed to separate MoS_2 flakes from bulk crystals. However, the lack of reproducibility in terms of lateral extension and thickness of the produced flakes make these approaches unsuitable for industrial applications in the field of electronics/optoelectronics. Differently, bottom-up approaches like Chemical Vapour Deposition (CVD) [16], Atomic Layer Deposition (ALD) [17], Pulsed Laser Deposition (PLD) [18,19], and Molecular Beam Epitaxy (MBE) [20] are more suitable to produce MoS_2 on large area in a scalable way. In particular, CVD is the most common and cost-effective method used in academic laboratories to obtain MoS_2 domains with good crystal quality by reaction of the precursor vapours, obtained by evaporation of sulfur (S) and molybdenum trioxide (MoO_3) powders, on the final substrate surface [21]. The process is typically carried out in a quartz-tube system with two heating zones, a low temperature one hosting the S crucible and a higher temperature one hosting the MoO_3 crucible and the substrate [22], while an inert gas is used for the transport of the evaporated species to the substrate surface [21]. Achieving an optimal MoS_2 growth by the CVD method requires

* Corresponding author.
E-mail address: Filippo.giannazzo@imm.cnr.it (F. Giannazzo).

https://doi.org/10.1016/j.mee.2023.111967
Received 30 January 2023; Received in revised form 22 February 2023; Accepted 2 March 2023
Available online 11 March 2023

the control of different parameters, including the amount of the Mo and S precursors [23–25], the carrier gas flow [26], and the temperature [27]. Furthermore, the substrates play a key role in the deposition mechanism [28–30], since their surface properties (e.g. roughness, crystalline or amorphous structure) have an impact on the MoS_2 domains nucleation and orientation. Although Si wafers coated by amorphous SiO_2 films are commonly employed as substrates for MoS_2 deposition, randomly oriented growth of MoS_2 domains is typically obtained on their surface, ultimately resulting in the formation of grain boundaries after domains merging [16,31,32]. On the other hand, crystalline α-Al_2O_3 (c-sapphire) is a suitable substrate for the rotationally aligned epitaxial growth of MoS_2, thanks to its high thermal stability, atomically flat surface, and hexagonal structure with good lattice constants matching to MoS_2 on the basal plane [33,34].

In the CVD process, the reaction leading to MoS_2 formation mainly occurs in the vapour phase, and the lateral growth of 1L-MoS_2 domains on the substrate occurs by attachment of the MoS_2 molecules starting from nucleation sites, resulting in the formation of flakes with typical triangular or hexagonal geometries, depending on the Mo:S precursors ratio and the growth temperature [35]. The growth of MoS_2 overlayers on the central region of the MoS_2 triangular flakes can be also observed, depending on the precursors flows during the CVD process [36]. Despite the very good quality and large size (from ~1 μm to ~100 μm size) of the MoS_2 flakes obtained by the CVD approach, several improvements are necessary to control the thickness uniformity and to achieve uniform MoS_2 coverage on wafer scale [37,38].

An alternative approach to the above-described single-step CVD is the sulfurization of a thin Mo (or MoO_x) film. In this method, also called two-step CVD growth, the first step consists in the deposition of the thin Mo (or MoO_x) film on the substrate by a physical vapour deposition (PVD) technique, such as electron-beam evaporation or magnetron sputtering, while the second step is represented by a thermal treatment of the sample under sulfur flux to convert the pre-deposited film into MoS_2 [39,40]. Also in this case, the sulfurization process is typically carried out in a two-zones tube furnace, where the S vapours, evaporated from a crucible in the low-temperature zone, are transported by the carrier gas to the second zone, hosting the sample coated by the Mo (or MoO_x) film. Differently than in the single-step CVD, where MoS_2 formation already occurs by precursors reaction in the vapour phase, in the case of the sulfurization approach the dominant mechanism leading to MoS_2 formation is typically represented by the vapour-solid heterogeneous reaction between the S gas and the solid MoO_x film [40]. The conversion of the pre-deposited film into MoS_2 allows to achieve optimal MoS_2 coverage and thickness uniformity on large areas (even on wafer scale), by controlling the starting pre-deposited film thickness. On the other hand, MoS_2 layers obtained by the sulfurization approach typically exhibit a nanocrystalline structure, originating from the nano-grains morphology of PVD deposited Mo or MoO_x films, which negatively affects the mobility of a MoS_2-based device. The structure of the MoS_2 films obtained by sulfurization process has been demonstrated to be strongly dependent on the thickness of the starting MoO_x films. In fact, while in the case of ultra-thin pre-deposited films S vapours directly react with the exposed MoO_x surface, for thicker ones (> 3 nm) the diffusion of S atoms inside the film represents the limiting mechanism of the process [41]. As a result, while MoS_2 layers horizontally aligned with the substrate are typically obtained from ultra-thin MoO_x films, the formation of vertically standing MoS_2 has been observed for thick pre-deposited MoO_x, as this configuration allows an easier penetration of S atoms in the inner part of the film [42,43].

The sulfurization process has been demonstrated to occur on a large range of temperatures between 500 °C and 1000 °C [40]. Obviously, besides the above-discussed vapour-solid reaction, additional physical mechanisms become relevant in the MoS_2 formation, depending on the temperature process and other parameters, such as the pressure, the local S concentration and the heating rate of the substrate [44,45]. In fact, considering that the sublimation temperature of MoO_3 is around 700 °C [40], the evaporation of MoO_x from the surface becomes increasingly important at temperatures higher than this value, resulting in a competitive mechanism with the MoO_x surface diffusion on the substrate and with the vapour-solid sulfurization reaction.

In this work, we report on the formation of micrometer-size crystalline 1L-MoS_2 triangular flakes with a central multilayer core, obtained on a c-sapphire substrate by sulfurization of ultrathin sputter-deposited MoO_x films (with thickness ranging from 1.2 and 1.8 nm) at a temperature of 800 °C. The structural, optical, and vibrational properties of these MoS_2 triangular flakes have been extensively investigated by different techniques with micro- and nanoscale resolution. Starting from optical microscopy and transmission electron microscopy (TEM) analyses, an explanation of the triangular MoS_2 flakes formation mechanism is proposed. The thickness uniformity, strain and doping of MoS_2 induced by the growth conditions and by the interaction with the substrate have been evaluated and correlated by micro-Raman spectroscopy. The 1L-MoS_2 flakes on the c-sapphire surface obtained by these sulfurization conditions have been shown to exhibit intense PL emission at ~1.85 eV, indicating a crystalline quality comparable to flakes produced by the conventional single-step CVD.

2. Materials and methods

2.1. Materials growth

The starting MoO_x films on the c-sapphire substrate were obtained by DC magnetron sputtering from a Mo target using a Quorum Q300-TD Plus equipment, followed by natural oxidation in air [46,47]. The thickness of these films (in the range between 1.2 and 1.8 nm) was evaluated by AFM step-height measurements. Afterwards, the sulfurization process to convert MoO_x into MoS_2 was carried out in a two-heating zone furnace, placing the crucible with the sulfur powder (~130 mg) in the low-temperature zone (at 150 °C) and the MoO_x/sapphire sample in the high temperature zone (at 800 °C), respectively. A constant flux (100 sccm) of Ar carrier gas was employed to transport the sulfur vapour from the first to the second zone. The growth was carried out at a base pressure of $\sim 4 \times 10^{-6}$ bar for 1 h.

2.2. TEM characterization

High resolution transmission electron microscopy (HR-TEM) and high angle annular dark field scanning transmission electron microscopy (HAADF-STEM) analyses of the MoS_2 flakes on sapphire were carried out with an aberration-corrected Titan Themis 200 microscope by Thermo Fisher. To this aim, cross-sectioned samples were prepared by a focused ion beam (FIB).

2.3. Vibrational and optical characterization

Micro-Raman maps were collected by a WiTec Alpha equipment, using a laser excitation at 532 nm, 1.5 mW power, and 100× objective. Furthermore, a Horiba HR-Evolution μ-Raman system with a laser excitation wavelength of 532 nm (nominal maximum power 100 mW) in a confocal configuration (100× objective) was employed to collect both μRaman and μPL spectra. A grating of 1800 lines/mm was employed to acquire Raman spectra in a range between 150 and 650 cm^{-1}, while a grating of 600 lines/mm was employed to acquire the μ-PL spectra in a range between 10 and 5500 cm^{-1}. In both the configurations, the laser power was filtered with a neutral density filter at 1%.

3. Results and discussion

3.1. Structure of MoS_2 flakes and growth mechanisms

Fig. 1 reports a representative optical image of MoS_2 flakes obtained by the 800 °C sulfurization of the thin MoO_x films on sapphire. These

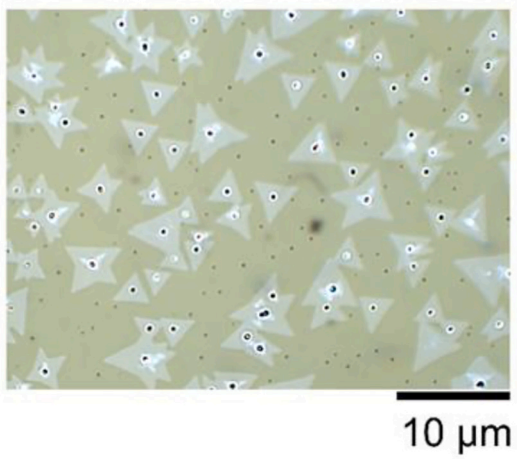

Fig. 1. Representative optical image of the MoS_2 samples obtained by sulfurization of MoO_x films at 800 °C.

flakes typically exhibit triangular shapes with a lateral size of around 3–5 μm, and, in some cases, irregular and stars-shaped flakes, resulting from the coalescence of adjacent smaller triangles. A small core region with a different optical contrast can be typically observed at the centre of the flakes, suggesting the presence of a different number of layers in the core with respect to the surrounding part of the triangle. As discussed more in depth later on in this paper, these core regions correspond to few layers MoS_2 islands formed at the beginning of the sulfurization process. These islands worked as nucleation centres for the lateral growth of the MoS_2 flakes, occurring by diffusion of MoO_x species on the sapphire surface, their attachment to the original nuclei and conversion to MoS_2 by the sulfurization reaction. In this respect, the lateral size of the flakes is limited by the loss of MoO_x from the surface, due to the competing evaporation phenomena.

Further information on the crystalline quality and thickness uniformity of the triangular flakes are obtained by Raman spectroscopy. A typical Raman spectrum of the MoS_2 on c-sapphire is reported in Fig. 2 (a), where the in-plane (E_{2g}), the out-of-plane (A_{1g}) and the second-order longitudinal acoustic (2LA(M)) modes exhibit much higher intensity with respect to the vibrational mode of the c-sapphire substrate, whose position is indicated by the blue arrow. Noteworthy, the first-order longitudinal peak (LA(M)) in the region between 100 and 300

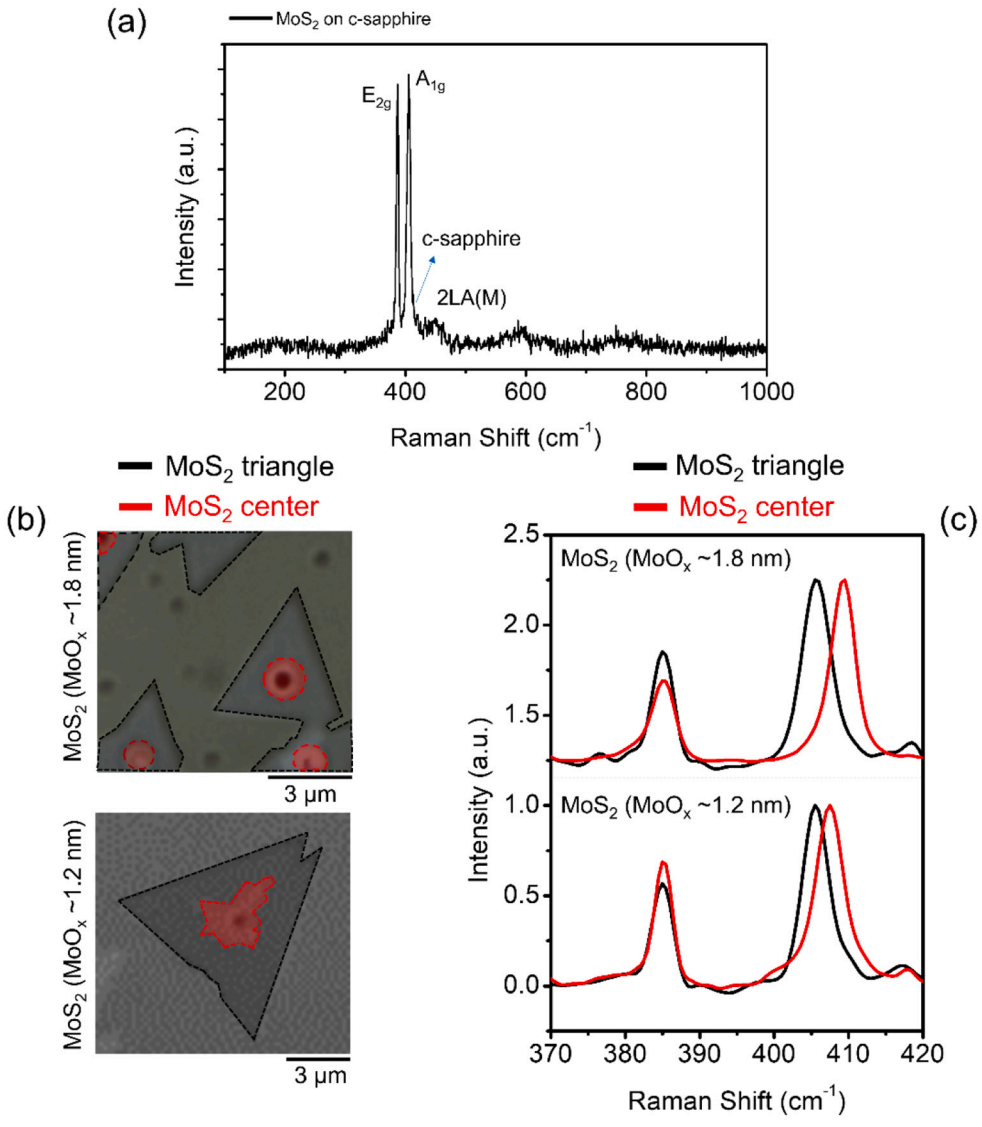

Fig. 2. (a) Typical Raman spectrum of MoS_2 on c-sapphire showing the typical E_{2g}, A_{1g} and 2LA(M) peaks. (b) Optical images of the MoS_2 flakes obtained from the thinner (bottom image) and thicker (upper image) MoO_x starting deposited films. The red area indicates the core of the flakes, while the black area indicates its base. (c) Corresponding Raman spectra of the center (red lines) and the base (black lines) of the MoS_2 obtained from the thinner (bottom spectra) and thicker (upper spectra, arbitrarily vertically shifted) MoO_x starting films.

cm^{-1}, typically associated with the presence of defects [48], is absent in these spectra, indicating a good crystal quality of the MoS_2 flakes obtained in these growth conditions.

In addition, both the E_{2g} and A_{1g} peaks show a very low Full Width at Half Maximum (FWHM, in a range between 2.4 and 3.6 cm^{-1}) and high E_{2g}/A_{1g} intensity ratios (0.5–0.7) comparable to those revealed in mechanical exfoliated and single-step CVD growth flakes, providing a further confirmation of the very good MoS_2 crystal quality [49]. The optical images reported in Fig. 2(b) are two examples of MoS_2 flakes resulting from the sulfurization of MoO_x films with ~1.2 nm (bottom image) and ~ 1.8 nm (upper image) thickness.

Fig. 2(c) shows the comparison of Raman spectra collected in the central region (red lines) and in the outer region (black line) of the triangular flakes for the two samples. For a better comparison, all the spectra were normalized with respect to the A_{1g} peak intensity. The E_{2g} and A_{1g} peaks were fitted by Gaussian functions and the extracted information have been summarized in Table 1.

For both samples, the E_{2g} peaks are at the same frequency in all the regions, whereas the separation ($\Delta\omega = \omega_{A1g} - \omega_{E2g}$) between the two peaks' frequencies is higher in the central core (red spectra) compared to the remaining part of the flakes (black spectra), consistently with a larger MoS_2 thickness in the core region. Noteworthy, the same value of $\Delta\omega \sim 20.5$ cm^{-1}, consistent with 1L-MoS_2 thickness [14], was obtained in the triangular region of the flakes. Differently, we estimated a $\Delta\omega \sim 22.4$ cm^{-1} and ~ 24.1 cm^{-1} in the central regions of the flakes obtained from the thinner and thicker MoO_x films, corresponding to 2L/3L and multilayer MoS_2 thickness, respectively.

Hence, Raman analyses showed that the thinner triangular region of the flakes consists of 1L-MoS_2, independently of the initial MoO_x thickness, whereas the central core regions are thicker for the sample with the thicker initial MoO_x thickness.

To better understand the structure of the MoS_2 triangular domains, cross-sectional TEM analyses have been performed close to the central part of the flakes, as shown in Fig. 3(a). This image confirms that the core is composed by few layers MoS_2, which becomes thinner until reaching 1L-MoS_2 thickness in the remaining part of the flake. The STEM-HAADF image in Fig. 3(b) allowed to precisely evaluate the number of MoS_2 layers in the core region (i.e. 3L-MoS_2), by direct visualization of the high *Z*-contrast Mo atoms (bright layers) and the lower *Z*-contrast of Al atoms of the c-sapphire substrate. The insert of Fig. 3(a) is a high magnification view of the boundary between the core and the thin region of the flake. The configuration of the layers, schematically illustrated in Fig. 3(c) and (d), provides interesting insights on the formation mechanisms of the flakes during the used sulfur annealing process, suggesting that the thin flake region is formed starting from a pre-existing few-layers MoS_2 core. Such a scenario is different from the one observed during the single-step CVD, where the formation of overlayers in the central region occurs after the formation of the 1L-MoS_2 flake.

Hence, basing on these observations, different competing phenomena can be considered to explain the formation of the triangular MoS_2 flakes during the sulfur annealing process at 800 °C. Starting from the uniform pre-deposited MoO_x film, diffusion of MoO_x species on the sapphire surface and their partial evaporation are probabily the main mechanisms before the reaction with the incoming S vapours. Clusterization of diffusing MoO_x is expected to occur at several positions on the substrate, leading to the formation MoO_x islands, which are converted into the multilayer MoS_2 cores by reaction with the incoming S vapours. These core structures represent the nucleation centers for the lateral growth of 1L-MoS_2 flakes, by attachement of diffusing MoO_x and solid-vapour reaction with S. The occurrence of vapour phase reaction between part of the evaporated MoO_x and incoming S close to the sample surface cannot be excluded as an additional formation mechanism of MoS_2 molecules attaching to the growing triangular flakes.

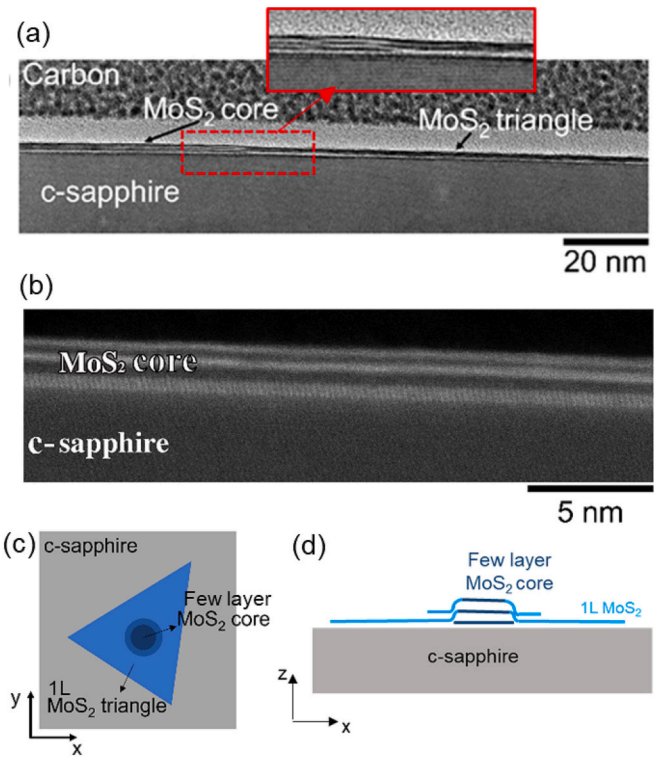

Fig. 3. (a) TEM image of the MoS_2 sample showing the presence of a central core and a thinner edge. (b) High magnification of the MoS_2 core of Fig. 3(a) in STEM-HAADF mode, showing three layers of MoS_2 on c-sapphire. (c) Scheme of the triangular-shaped MoS_2 flakes and its composition in the in-plane and (d) in the cross-section direction.

3.2. *Thickness homogeneity, strain, and doping evaluation of MoS_2 flakes*

After these preliminary analyses, we carried out different Raman maps on the two samples with the aim of extract further information related to the thickness homogeneity, strain and doping effects. The MoS_2 flakes appear in both cases composed by a central nucleus with high values of $\Delta\omega$ (higher than 21.5 cm^{-1}) corresponding to multilayers,

Table 1
Raman peaks information extracted from Gaussian fits of the two samples in the core and triangular part of the MoS_2 flakes. The error in each reported data is one digit in the least significant number.

	Starting MoO_x thickness	E_{2g} (cm^{-1})	FWHM E_{2g} (cm^{-1})	A_{1g} (cm^{-1})	FWHM A_{1g} (cm^{-1})	$\Delta\omega$ (cm^{-1})	Intensity ratio (a.u.)
Triangle	1.2 nm	385.0	2.6	405.5	3.1	20.5	0.6
Center	1.2 nm	385.1	2.4	407.5	3.1	22.4	0.7

	Starting MoO_x thickness	E_{2g} (cm^{-1})	FWHM E_{2g} (cm^{-1})	A_{1g} (cm^{-1})	FWHM A_{1g} (cm^{-1})	$\Delta\omega$ (cm^{-1})	Intensity ratio (a.u.)
Triangle	1.8 nm	385.1	2.8	405.6	3.6	20.6	0.5
Center	1.8 nm	385.2	2.8	409.3	2.8	24.1	0.5

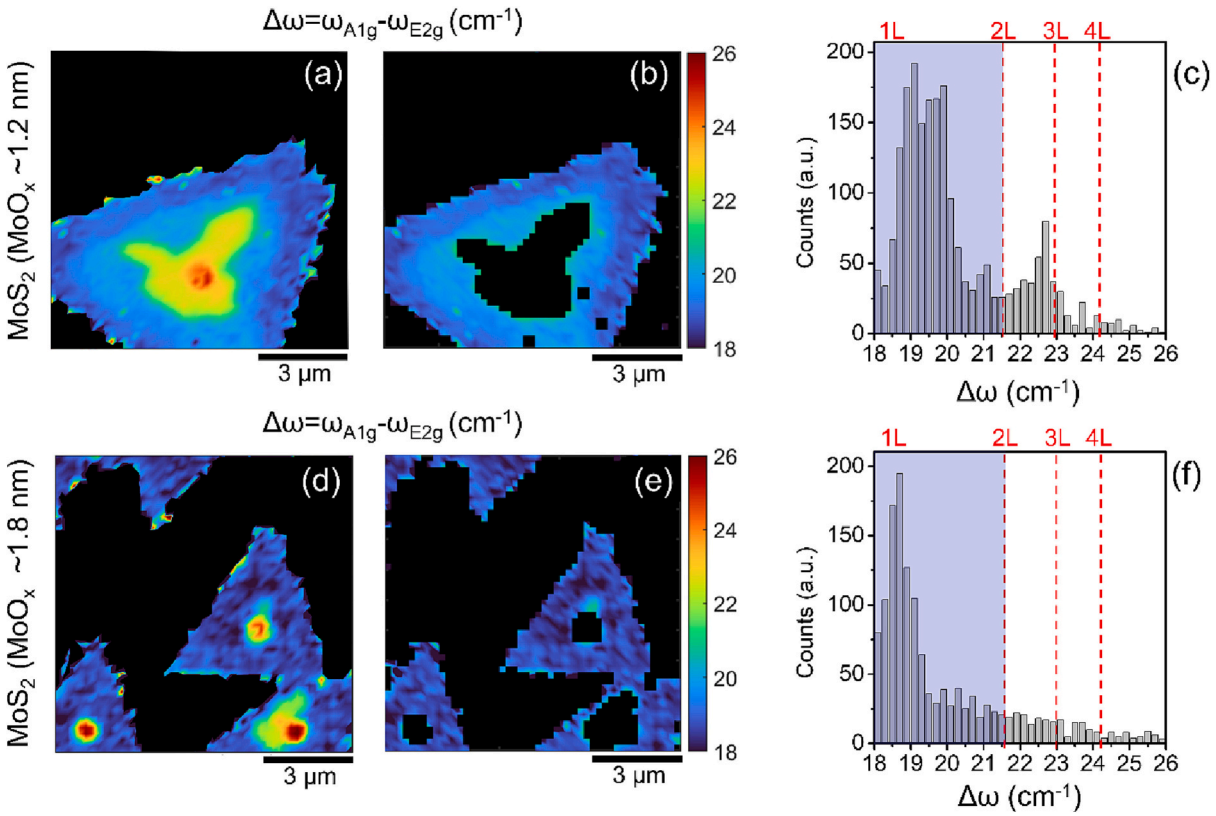

Fig. 4. (a) Raman map of the difference between the two MoS_2 vibrational modes ($\Delta\omega = \omega_{A1g}$-$\omega_{E2g}$) of the sample obtained from 1.2 nm of MoO_x. (b) Same Raman map of Fig. 4(a) in which the thicker parts of the flakes ($\Delta\omega > 21.5$ cm^{-1}) are removed. (c) Corresponding histogram of $\Delta\omega$ for the Raman map in Fig. 4(a), in which the blue area indicated the only part considered in Fig. 4(b). (d) Raman map of the difference between the two MoS_2 vibrational modes ($\Delta\omega = \omega_{A1g}$-$\omega_{E2g}$) of the sample obtained from 1.8 nm of MoO_x. (e) Same Raman map of Fig. 4(d) in which the thicker parts of the flakes ($\Delta\omega > 21.5$ cm^{-1}) are removed. (f) Corresponding histogram of $\Delta\omega$ for the Raman map in Fig. 4(d), in which the blue area indicated the part considered in Fig. 4(e).

as shown in Fig. 4(a,d). $\Delta\omega$ decreases moving away from the central part (red, yellow and green region) and approaching to the base of the flakes (light blue and blue region), where a minimum value of 18 cm^{-1} is observed, matching with a 1L-MoS_2. In this sense, the structure of the flakes illustrated in Fig. 3(d) is confirmed, and it is more visible in Fig. 4 (a). Thus, the MoS_2 flakes figure like a monolayer base laterally extended few tens of micrometres with a smaller central nucleus composed by few layers of MoS_2. The black background in the $\Delta\omega$ maps is due to the absence of MoS_2 Raman signals around the triangular flakes. The $\Delta\omega$ distributions in Fig. 4(c,f) appear mainly centred in the region between 18 and 21.5 cm^{-1}, corresponding to a monolayer (underlined by the blue rectangles), and further bumps are visible for $\Delta\omega > 21.5$ cm^{-1}, associated to the multilayers component in the central part of the flakes. Behind the evaluation of the MoS_2 thickness, Raman peaks can give further information about the strain and doping effects induced by the growth conditions and the interaction with the substrate [14,50,51]. For this purpose, we will focus the attention only on the effects induced on the 1L-MoS_2, removing the multilayer part as shown in Fig. 4(b,e). The correlation between the MoS_2 vibrational modes and the strain and doping parameters is expressed by the following equation:

$$\omega_m = \omega_m^0 - 2\gamma_m\omega_m^0\varepsilon + k_m n \quad (1)$$

where ω_m represent the experimental positions for each vibrational modes (m = E_{2g}, A_{1g}), while ω_m^0 terms are the reference positions for each mode in the unstrained and undoped 1L-MoS_2 configuration. To this aim, the literature values of the Raman peaks for a 1L-MoS_2 suspended (ω_{E2g}= 385 cm^{-1} and ω_{A1g}= 405 cm^{-1}) have been chosen as the best approximation for the ideal unstrained and undoped set [52]. Finally, γ_m and k_m represent the Grüneisen parameters and the shift-rate of the Raman peaks as a function of the electron density (n) of the 1L-MoS_2, respectively [14,52,53,54].

The corresponding strain and doping maps of the previous reported $\Delta\omega$ maps of Fig. 4(b,e) are reported in Fig. 5(a,e) and Fig. 5(c,g) respectively. The strain maps of the two samples showed local variation in a range between $-1\ \% < \varepsilon < 1\ \%$, demonstrated by the slight colour change. The corresponding strain distribution of the 1L-MoS_2 sample obtained from the thinner MoO_x film (~1.2 nm), reported in Fig. 5(b), is peaked near the ideal value of the suspended 1L-MoS_2 membrane, but showed a compressive strain with a mean value of $\varepsilon_{comp} \approx 0.13 \pm 0.23$ %. In contrast to this, the sample obtained from the thicker MoO_x film (~1.8 nm) appeared more stressed and subjected to a mean compression of $\varepsilon_{comp} \approx 0.39 \pm 0.24\%$, as shown in Fig. 5(f). Differently from the previous evaluation, the inhomogeneity of the carrier concentration in the two samples is just appreciable by the corresponding doping maps, whose colour variations appear very pronounced. Interestingly, there is a parallelism between the previous variation of $\Delta\omega$ in Fig. 4(b) and that of doping in Fig. 5(c). In fact, approaching to the center of the sample, the variation of the doping matches perfectly with the previous $\Delta\omega$ change, but that is not observed in the corresponding strain map in Fig. 5 (a). Thus, the $\Delta\omega$ variation can be associated mainly to a doping effect rather than strain effect on the thin MoS_2 flake. To do a better evaluation of the doping levels, the doping distributions of the two samples are reported in Fig. 5(d,h). The histogram reported in Fig. 5(d) exhibited a doping ranging from -1.5×10^{13} cm$^{-2} < n < 2.5 \times 10^{13}$ cm^{-2}, with a pronounced peak in the n-type region (orange rectangle) with a mean value of $n \approx (0.33 \pm 0.61) \times 10^{13}$ cm^{-2}. This value is in good agreement with the n-type doping derived in 1L-MoS_2 supported by insulating substrates (obtained by mechanical exfoliation or CVD) [55–58]. Similarly, the MoS_2 sample obtained from the thicker MoO_x film (~1.8 nm)

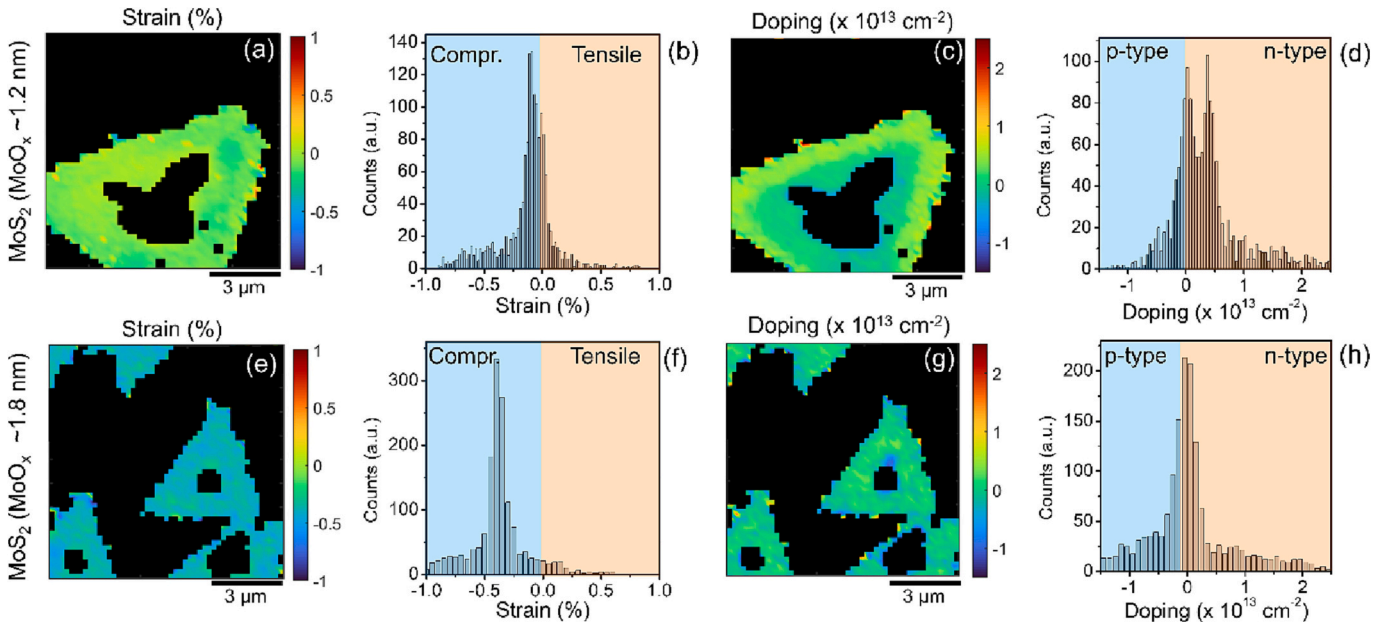

Fig. 5. Corresponding strain maps on the MoS_2 samples obtained from (a) MoO_x of 1.2 nm and (e) 1.8 nm from Fig. 4(b-e). Histogram distribution of strain of the MoS_2 samples obtained from (b) MoO_x of 1.2 nm and (f) 1.8 nm. Corresponding doping maps on the MoS_2 samples obtained from (c) MoO_x of 1.2 nm and (g) 1.8 nm from Fig. 4(b-e). Histogram distribution of doping of the MoS_2 samples obtained from (d) MoO_x of 1.2 nm and 1.8 nm (h).

showed a doping distributed in the same range, but the single peak is very near the ideal undoped condition. This effect is translated in a lower mean n-type doping value of $n \approx (0.08 \pm 0.69) \times 10^{13}$ cm^{-2}.

The optical properties of the two samples were analysed by μ-Photoluminescence spectroscopy. The 1L-MoS_2 (base of the triangle) showed the more intense peak centred at around 1.85 eV in both samples, as represented by the black spectra in Fig. 6(a-b). By contrast, the MoS_2 sample obtained from the thinner MoO_x film central part showed a decrease of the PL intensity, as shown in Fig. 6(a), while the other one undergoes a total quenching, as represented by the red curve in Fig. 6(b). These two different effects are in perfect agreement with the previous Raman results, because the first sample showed a $\Delta\omega \approx 22.4$ cm^{-1} comparable with few-layers MoS_2, in which the band structure has some variations but there is not yet a complete transition to an indirect band gap, as that in the bulk form for the second sample ($\Delta\omega \approx 24.1$ cm^{-1}). For both samples a statistical analysis has been carried out, from which were extracted the mean values of the PL peaks, as shown in Fig. 6(c), exhibiting a perfect matching in the two cases ($x_{PL1} \approx 1.84 \pm 0.02$ eV and $x_{PL2} \approx 1.85 \pm 0.01$ eV). Finally, supposing the suspended 1L-MoS_2 as the closest condition to the ideal unstrained and undoped 1L-MoS_2, it was possible to extract the corresponding biaxial strain considering an experimental and a theoretical PL shift rate as a function of the strain of about −99 meV/% and − 105 meV/%, respectively [52,59]. From our PL experimental results, we deducted a biaxial strain of around 0.4%

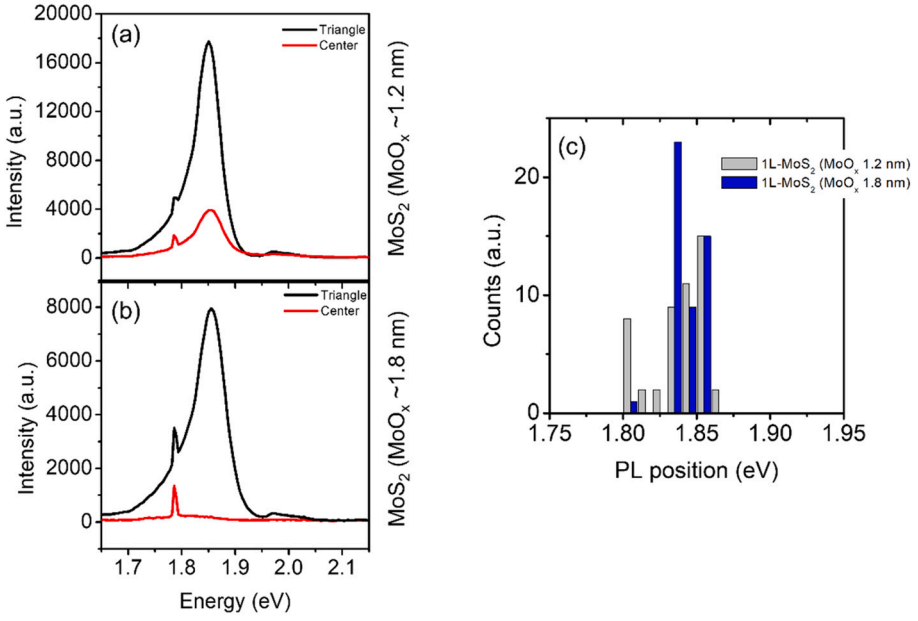

Fig. 6. (a) Photoluminescence spectra of the MoS_2 triangle (black line) and center (red line) obtained from 1.2 nm MoO_x film. (b) Photoluminescence spectra of the MoS_2 triangle (black line) and center (red line) obtained from 1.8 nm MoO_x film. (c) Statistical distribution of the PL peaks in both the samples.

and 0.38% that are in perfect agreement with the strain values extrapolated from the previous Raman measurements.

4. Conclusion

We have demonstrated the formation of micrometer-size crystalline monolayer (1L) MoS_2 flakes with triangular shape and a central multilayer core by the sulfurization at 800 °C of pre-deposited ultrathin MoO_x films (1.2–1.8 nm) on c-sapphire substrates. Both μ-Raman and TEM/STEM analysis confirmed the formation of the thicker central core supported by micrometer-extended triangular 1L-MoS_2. The different starting MoO_x films appear to mainly influence the core thickness, showing the presence of ~3L- and multilayers MoS_2 from 1.2 nm and 1.8 nm MoO_x, respectively. These MoS_2 flakes showed an excellent crystalline quality comparable with those obtained from single-step CVD approach, as demonstrated by μ-Raman (small FWHM of the Raman peaks) and μ-PL characterizations (high intensity peak centred at 1.85 eV). Based on these evaluations, different competitive phenomena are expected to occur in order to achieve MoS_2 flakes from the MoO_x films at these growth conditions. Raman mapping was exploited to evaluate the thickness uniformity, the strain and doping effects of the two samples. In particular, the MoS_2 flakes obtained from the thinner MoO_x film (1.2 nm) appear near the ideal strain of the suspended MoS_2 membrane (0.13 ± 0.23%) and with a n-type doping of $(0.33 \pm 0.61) \times 10^{13}$ cm^{-2}. Differently, the MoS_2 flakes obtained from the thicker MoO_x film (1.8 nm) appear subjected to a biaxial compressive strain of 0.39 ± 0.24%, but with a n-type doping near the ideal condition of the suspended MoS_2 membrane ($(0.08 \pm 0.69) \times 10^{13}$ cm^{-2}). μ-PL showed the typical decrease of the PL intensity as a function of the thickness, reaching a total quenching for the multilayers MoS_2. Finally, from μ-PL results, a biaxial strain of 0.38–0.4%, was deducted in perfect agreement with the previous Raman results.

The sulfurization of sputter-deposited MoO_x films is a facile process, highly compatible with the semiconductor devices fabrication flow. Hence, the demonstrated possibility of obtaining high crystalline quality MoS_2 on sapphire by this approach offers significant advantages in the perspective of wafer scale MoS_2 integration for microelectronics and optoelectronics, e.g. ultra-thin channel transistors and photodetectors.

CRediT authorship contribution statement

S.E. Panasci: Investigation, Formal analysis, Writing – review & editing. **E. Schilirò:** Investigation, Formal analysis, Writing – review & editing. **A. Koos:** Investigation, Writing – review & editing. **M. Nemeth:** Investigation, Writing – review & editing. **M. Cannas:** Resources, Writing – review & editing. **S. Agnello:** Resources, Writing – review & editing. **F. Roccaforte:** Project administration, Writing – review & editing. **B. Pécz:** Funding acquisition, Investigation, Writing – review & editing. **F. Giannazzo:** Conceptualization, Funding acquisition, Project administration, Supervision, Writing – original draft, Writing – review & editing.

Declaration of Competing Interest

The authors declare that they have no known competing financial interests or personal relationships that could have appeared to influence the work reported in this paper.

Data availability

Data will be made available on request.

Acknowledgements

S. Di Franco (CNR-IMM) is acknowledged for his expert assistance with samples preparation, and F. M. Gelardi (Univ. of Palermo) for useful discussion. This work has been supported, in part, by MUR in the framework of the FlagERA JTC 2019 project ETMOS. Funding for travels from CNR/HAS (2023-25) bilateral project GHOST-III is acknowledged. This work has been partially funded by European Union (NextGeneration EU), through the MUR-PNRR project SAMOTHRACE (ECS00000022).

References

[1] K.F. Mak, C. Lee, J. Hone, J. Shan, T.F. Heinz, Atomically thin MoS_2: a new direct-gap semiconductor, Phys. Rev. Lett. 105 (13) (2010), 136805, https://doi.org/10.1103/PhysRevLett.105.136805.
[2] A. Splendiani, L. Sun, Y. Zhang, T. Li, J. Kim, C.Y. Chim, G. Galli, F. Wang, Emerging photoluminescence in monolayer MoS_2, Nano Lett. 10 (4) (2010) 1271–1275, https://doi.org/10.1021/nl903868w.
[3] B. Radisavljevic, M.B. Whitwick, A. Kis, Integrated circuits and logic operations based on single-layer MoS_2, ACS Nano 5 (2011) 9934–9938, https://doi.org/10.1021/nn203715c.
[4] O. Lopez-Sanchez, D. Lembke, M. Kayci, A. Radenovic, A. Kis, Ultrasensitive photodetectors based on monolayer MoS_2, Nat.Nanotechnol. 8 (2013) 497–501, https://doi.org/10.1038/nnano.2013.100.
[5] J. Hu, L. Yu, J. Deng, Y. Wang, K. Cheng, C. Ma, Q. Zhang, W. Wen, S. Yu, Y. Pan, et al., Sulfur vacancy-rich MoS_2 as a catalyst for the hydrogenation of CO_2 to methanol, Nat. Catal. 4 (2021) 242–250, https://doi.org/10.1038/s41929-021-00584-3.
[6] H. Li, Z. Yin, Q. He, H. Li, X. Huang, G. Lu, D.W.H. Fam, A.L.Y. Tok, Q. Zhang, H. Zhang, Fabrication of single-and multilayer MoS_2 film-based field-effect transistors for sensing NO at room temperature, Small 8 (2012) 63–67, https://doi.org/10.1002/smll.201101016.
[7] B. Radisavljevic, A. Radenovic, J. Brivio, V. Giacometti, A. Kis, Single-layer MoS_2 transistors, Nat. Nanotechnol. 6 (3) (2011) 147–150, https://doi.org/10.1038/nnano.2010.279.
[8] W. Wu, D. De, S.C. Chang, Y. Wang, H. Peng, J. Bao, S.S. Pei, High mobility and high on/off ratio field-effect transistors based on chemical vapor deposited single-crystal MoS_2 grains, Appl. Phys. Lett. 102 (2013), 142106, https://doi.org/10.1063/1.4801861.
[9] Y. Yoon, K. Ganapathi, S. Salahuddin, How good can monolayer MoS_2 transistors be? Nano Lett. 11 (2011) https://doi.org/10.1021/nl2018178, 3768–377.
[10] K.S. Novoselov, D. Jiang, F. Schedin, T.J. Booth, V.V. Khotkevich, S.V. Morozov, A. K. Geim, Two-dimensional atomic crystals, Proc. Natl. Acad. Sci. U. S. A. 102 (2005) 10451–10453, https://doi.org/10.1073/pnas.0502848102.
[11] C. Lee, H. Yan, L.E. Brus, T.F. Heinz, J. Hone, S. Ryu, Anomalous lattice vibrations of single-and few-layer MoS_2, ACS Nano 4 (2010) 2695–2700, https://doi.org/10.1021/nn1003937.
[12] G.Z. Magda, J. Pető, G. Dobrik, C. Hwang, L.P. Biró, L. Tapasztó, Exfoliation of large-area transition metal chalcogenide single layers, Sci. Rep. 5 (2015) 14714, https://doi.org/10.1038/srep14714.
[13] M. Velický, G.E. Donnelly, W.R. Hendren, S. McFarland, D. Scullion, W.J. I. DeBenedetti, G.C. Correa, Y. Han, A.J. Wain, M.A. Hines, D.A. Muller, K. S. Novoselov, H.D. Abruña, R.M. Bowman, E.J.G. Santos, F. Huang, Mechanism of gold- assisted exfoliation of centimeter-sized transition-metal dichalcogenide monolayers, ACS Nano 12 (2018) 10463–10472, https://doi.org/10.1021/acsnano.8b06101.
[14] S.E. Panasci, E. Schilirò, G. Greco, M. Cannas, F.M. Gelardi, S. Agnello, F. Roccaforte, F. Giannazzo, Strain, doping, and electronic transport of large area monolayer MoS2 exfoliated on gold and transferred to an insulating substrate, ACS Appl. Mater. Interfaces 13 (2021) 31248–31259, https://doi.org/10.1021/acsami.1c05185.
[15] J.N. Coleman, M. Lotya, A. O'Neill, S.D. Bergin, P.J. King, U. Khan, K. Young, A. Gaucher, S. De, R.J. Smith, et al., Two-dimensional nanosheets produced by liquid exfoliation of layered materials, Science 331 (2011) 568–571, https://doi.org/10.1126/science.1194975.
[16] Y.H. Lee, X.Q. Zhang, W. Zhang, M.T. Chang, C.T. Lin, K.D. Chang, Y.C. Yu, J.T. W. Wang, C.S. Chang, L.J. Li, T.S. Lin, Synthesis of large-area MoS_2 atomic layers with chemical vapor deposition, Adv. Mater. 24 (2012) 2320–2325, https://doi.org/10.1002/adma.201104798.
[17] A. Valdivia, D.J. Tweet, J.F. Conley Jr., Atomic layer deposition of two dimensional MoS_2 on 150 mm substrates, J. Vac. Sci. Technol. 34 (2016) 21515, https://doi.org/10.1116/1.4941245.
[18] Y.T. Ho, C.H. Ma, T.T. Luong, L.L. Wei, T.C. Yen, W.T. Hsu, W.H. Chang, Y.C. Chu, Y.Y. Tu, K.P. Pande, E.Y. Chang, Layered MoS_2 grown on c-sapphire by pulsed laser deposition, Phys. Status Solid (RRL)–Rapid Res. Lett. 9 (3) (2015) 187–191, https://doi.org/10.1002/pssr.201409561.
[19] F. Giannazzo, S.E. Panasci, E. Schilirò, P. Fiorenza, G. Greco, F. Roccaforte, M. Cannas, S. Agnello, A. Koos, B. Pécz, M. Španková, Š. Chromik, Highly homogeneous 2D/3D heterojunction diodes by pulsed laser deposition of MoS2 on ion implantation doped 4H-SiC, Adv. Mater. Interfaces 10 (2023) 2201502, https://doi.org/10.1002/admi.202201502.
[20] D. Fu, X. Zhao, Y.Y. Zhang, L. Li, H. Xu, A.R. Jang, S.I. Yoon, P. Song, S.M. Poh, T. Ren, Z. Ding, W. Fu, T.J. Shin, H.S. Shin, S.T. Pantelides, W. Zhou, K.P. Loh, Molecular beam epitaxy of highly crystalline monolayer molybdenum disulfide on hexagonal boron nitride, J. Am. Chem. Soc. 139 (2017) 9392–9400, https://doi.org/10.1021/jacs.7b05131.

[21] Y. Zhan, Z. Liu, S. Najmaei, P.M. Ajayan, J. Lou, Large-area vapor-phase growth and characterization of MoS_2 atomic layers on a SiO_2 substrate, Small 8 (2012) 966–971, https://doi.org/10.1002/smll.201102654.

[22] H.F. Liu, S.L. Wong, D.Z. Chi, CVD growth of MoS_2-based two-dimensional materials, Chem. Vap. Depos. 21 (10−11−12) (2015) 241–259, https://doi.org/10.1002/cvde.201500060.

[23] P. Kumar, B. Viswanath, Effect of sulfur evaporation rate on screw dislocation driven growth of MoS_2 with high atomic step density, Cryst. Growth Des. 16 (12) (2016) 7145–7154, https://doi.org/10.1021/acs.cgd.6b01367.

[24] A. Ubaldini, J. Jacimovic, N. Ubrig, E. Giannini, Chloride-driven chemical vapor transport method for crystal growth of transition metal dichalcogenides, Cryst. Growth Des. 13 (10) (2013) 4453–4459, https://doi.org/10.1021/cg400953e.

[25] G.H. Han, N.J. Kybert, C.H. Naylor, B.S. Lee, J. Ping, J.H. Park, J. Kang, S.Y. Lee, R. Agarwal, A.T. Johnson, Seeded growth of highly crystalline molybdenum disulphide monolayers at controlled locations, Nat. Commun. 6 (1) (2015) 1–6, https://doi.org/10.1038/ncomms7128.

[26] Y. Cao, X. Luo, S. Han, C. Yuan, Y. Yang, Q. Li, T. Yu, S. Ye, Influences of carrier gas flow rate on the morphologies of MoS_2 flakes, Chem. Phys. Lett. 631 (2015) 30–33, https://doi.org/10.1016/j.cplett.2015.05.001.

[27] Z. Zhu, S. Zhan, J. Zhang, G. Jiang, M. Yi, J. Wen, Influence of growth temperature on MoS_2 synthesis by chemical vapor deposition, Mater. Res. Expr. 6 (9) (2019), 095011, https://doi.org/10.1088/2053-1591/ab2c19.

[28] H. Yin, X. Zhang, J. Lu, X. Geng, Y. Wan, M. Wu, P. Yang, Substrate effects on the CVD growth of MoS_2 and WS_2, J. Mater. Sci. 55 (3) (2020) 990–996, https://doi.org/10.1007/s10853-019-03993-9.

[29] S. Wang, M. Pacios, H. Bhaskaran, J.H. Warner, Substrate control for large area continuous films of monolayer MoS_2 by atmospheric pressure chemical vapor deposition, Nanotechnology 27 (8) (2016), 085604, https://doi.org/10.1088/0957-4484/27/8/085604.

[30] J. Sitek, J. Plocharski, I. Pasternak, A.P. Gertych, C. McAleese, B.R. Conran, M. Zdrojek, W. Strupinski, Substrate induced variances in morphological and structural properties of MoS_2 grown by chemical vapor deposition on epitaxial graphene and SiO_2, ACS Appl. Mater. Interfaces 12 (40) (2020) 45101–45110, https://doi.org/10.1021/acsami.0c06173.

[31] L. Seravalli, M. Bosi, P. Fiorenza, S.E. Panasci, D. Orsi, E. Rotunno, L. Cristofolini, F. Rossi, F. Giannazzo, F. Fabbri, Gold nanoparticle assisted synthesis of MoS_2 monolayers by chemical vapor deposition, Nanoscale Adv. 3 (2021) 4826, https://doi.org/10.1039/d1na00367d.

[32] F. Giannazzo, M. Bosi, F. Fabbri, E. Schilirò, G. Greco, F. Roccaforte, Direct probing of grain boundary resistance in chemical vapor deposition-grown monolayer MoS_2 by conductive atomic force microscopy, Phys. Status Solidi (RRL) 14 (2020) 1900393, https://doi.org/10.1002/pssr.201900393.

[33] Q. Ji, M. Kan, Y. Zhang, Y. Guo, D. Ma, J. Shi, Q. Sun, Q. Chen, Y. Zhang, Z. Liu, Unravelling orientation distribution and merging behavior of monolayer MoS_2 domains on sapphire, Nano Lett. 15 (1) (2015) 198–205, https://doi.org/10.1021/nl503373x.

[34] T. Li, W. Guo, L. Ma, W. Li, Z. Li, Z. Yu, Z. Han, S. Gao, L. Liu, D. Fan, Z. Wang, Y. Yang, W. Lin, Z. Luo, X. Chen, N. Dai, X. Tu, D. Pan, Y. Yao, P. Wang, Y. Nie, J. Wang, Y. Shi, X. Wang, Epitaxial growth of wafer-scale molybdenum disulfide semiconductor single crystals on sapphire, Nat. Nanotechnol. 16 (11) (2021) 1201–1207, https://doi.org/10.1038/s41565-021-00963-8.

[35] S.Y. Yang, G.W. Shim, S.B. Seo, S.Y. Choi, Effective shape-controlled growth of monolayer MoS_2 flakes by powder-based chemical vapor deposition, Nano Res. 10 (1) (2017) 255–262, https://doi.org/10.1007/s12274-016-1284-6.

[36] D. Zhou, H. Shu, C. Hu, L. Jiang, P. Liang, X. Chen, Unveiling the growth mechanism of MoS2 with chemical vapor deposition: from two-dimensional planar nucleation to self-seeding nucleation, Cryst. Growth Des. 18 (2) (2018) 1012–1019, https://doi.org/10.1021/acs.cgd.7b01486.

[37] S. Najmaei, J. Yuan, J. Zhang, P. Ajayan, J. Lou, Synthesis and defect investigation of two-dimensional molybdenum disulfide atomic layers, Acc. Chem. Res. 48 (1) (2015) 31–40, https://doi.org/10.1021/ar500291j.

[38] S. Najmaei, Z. Liu, W. Zhou, X. Zou, G. Shi, S. Lei, B.I. Yakobson, J.C. Idrobo, P. M. Ajayan, J. Lou, Vapour phase growth and grain boundary structure of molybdenum disulphide atomic layers, Nat. Mater. 12 (8) (2013) 754–759, https://doi.org/10.1038/nmat3673.

[39] Y.C. Lin, W. Zhang, J.K. Huang, K.K. Liu, Y.H. Lee, C.T. Liang, C.W. Chu, L.J. Li, Wafer-scale MoS_2 thin layers prepared by MoO_3 sulfurization, Nanoscale 4 (20) (2012) 6637–6641, https://doi.org/10.1039/C2NR31833D.

[40] S. Vangelista, E. Cinquanta, C. Martella, M. Alia, M. Longo, A. Lamperti, R. Mantovan, F.B. Basset, F. Pezzoli, A. Molle, Towards a uniform and large-scale deposition of MoS_2 nanosheets via sulfurization of ultra-thin Mo-based solid films, Nanotechnology 27 (17) (2016), 175703, https://doi.org/10.1088/0957-4484/27/17/175703.

[41] D. Kong, H. Wang, J.J. Cha, M. Pasta, K.J. Koski, J. Yao, Y. Cui, Synthesis of MoS_2 and $MoSe_2$ films with vertically aligned layers, Nano Lett. 13 (2013) 1341–1347, https://doi.org/10.1021/nl400258t.

[42] S.-Y. Cho, S.J. Kim, Y. Lee, J.-S. Kim, W.-B. Jung, H.-W. Yoo, J. Kim, H.-T. Jung, Highly enhanced gas adsorption properties in vertically aligned MoS_2 layers, ACS Nano 9 (2015) 9314–9321, https://doi.org/10.1021/acsnano.5b04504.

[43] Y. Jung, J. Shen, Y. Liu, J.M. Woods, Y. Sun, J.J. Cha, Metal seed layer thickness-induced transition from vertical to horizontal growth of MoS_2 and WS_2, Nano Lett. 14 (2014) 6842–6849, https://doi.org/10.1021/nl502570f.

[44] S.-L. Shang, G. Lindwall, Y. Wang, J.M. Redwing, T. Anderson, Z.-K. Liu, Lateral versus vertical growth of two-dimensional layered transition-metal dichalcogenides: thermodynamic insight into MoS_2, Nano Lett. 16 (2016) 5742–5750, https://doi.org/10.1021/acs.nanolett.6b02443.

[45] R. Shahzad, T. Kim, S.W. Kang, Effects of temperature and pressure on sulfurization of molybdenum nano-sheets for MoS_2 synthesis, Thin Solid Films 641 (2017) 79–86, https://doi.org/10.1016/j.tsf.2016.12.041.

[46] S.E. Panasci, A. Koos, E. Schilirò, S. Di Franco, G. Greco, P. Fiorenza, F. Roccaforte, S. Agnello, M. Cannas, F.M. Gelardi, A. Sulyok, M. Nemeth, B. Pécz, F. Giannazzo, Multiscale investigation of the structural, electrical and photoluminescence properties of MoS_2 obtained by MoO_3 sulfurization, Nanomaterials 12 (2) (2022) 182, https://doi.org/10.3390/nano12020182.

[47] F. Giannazzo, S.E. Panasci, E. Schilirò, F. Roccaforte, A. Koos, M. Nemeth, B. Pécz, Esaki diode behavior in highly uniform MoS_2/silicon carbide heterojunctions, Adv. Mater. Interfaces 9 (22) (2022) 2200915, https://doi.org/10.1002/admi.20220091.

[48] S. Mignuzzi, A.J. Pollard, N. Bonini, B. Brennan, I.S. Gilmore, M.A. Pimenta, D. Richards, D. Roy, Effect of disorder on Raman scattering of single-layer MoS_2, Phys. Rev. B 91 (19) (2015), 195411, https://doi.org/10.1103/PhysRevB.91.195411.

[49] C.R. Wu, X.R. Chang, C.H. Wu, S.Y. Lin, The growth mechanism of transition metal dichalcogenides by using sulfurization of pre-deposited transition metals and the 2D crystal hetero-structure establishment, Sci. Rep. 7 (1) (2017) 1–8, https://doi.org/10.1038/srep42146.

[50] W.H. Chae, J.D. Cain, E.D. Hanson, A.A. Murthy, V.P. Dravid, Substrate induced strain and charge doping in CVD grown monolayer MoS_2, Appl. Phys. Lett. 111 (14) (2017), 143106, https://doi.org/10.1063/1.4998284.

[51] A. Michail, N. Delikoukos, J. Parthenios, C. Galiotis, K. Papagelis, Optical detection of strain and doping inhomogeneities in single layer MoS_2, Appl. Phys. Lett. 108 (17) (2016), 173102, https://doi.org/10.1063/1.4948357.

[52] D. Lloyd, X. Liu, J.W. Christopher, L. Cantley, A. Wadehra, B.L. Kim, B.B. Goldberg, A.K. Swan, J.S. Bunch, Band gap engineering with ultralarge biaxial strains in suspended monolayer MoS_2, Nano Lett. 16 (9) (2016) 5836–5841, https://doi.org/10.1021/acs.nanolett.6b02615.

[53] B. Chakraborty, A. Bera, D.V.S. Muthu, S. Bhowmick, U.V. Waghmare, A.K. Sood, Symmetry-dependent phonon renormalization in monolayer MoS_2 transistor, Phys. Rev. B 85 (16) (2012), 161403, https://doi.org/10.1103/PhysRevB.85.161403.

[54] N. Ferralis, Probing mechanical properties of graphene with Raman spectroscopy, J. Mater. Sci. 45 (19) (2010) 5135–5149, https://doi.org/10.1007/s10853-010-4673-3.

[55] S.E. Panasci, E. Schiliro, F. Migliore, M. Cannas, F.M. Gelardi, F. Roccaforte, F. Giannazzo, S. Agnello, Substrate impact on the thickness dependence of vibrational and optical properties of large area MoS_2 produced by gold-assisted exfoliation, Appl. Phys. Lett. 119 (9) (2021), 093103, https://doi.org/10.1063/5.0062106.

[56] K.F. Mak, K. He, C. Lee, G.H. Lee, J. Hone, T.F. Heinz, J. Shan, Tightly bound trions in monolayer MoS_2, Nat. Mater. 12 (3) (2013) 207–211, https://doi.org/10.1038/nmat3505.

[57] S. Mouri, Y. Miyauchi, K. Matsuda, Tunable photoluminescence of monolayer MoS_2 via chemical doping, Nano Lett. 13 (12) (2013) 5944–5948, https://doi.org/10.1021/nl403036h.

[58] T. Komesu, D. Le, I. Tanabe, E.F. Schwier, Y. Kojima, M. Zheng, K. Taguchi, K. Miyamoto, T. Okuda, H. Iwasawa, K. Shimada, T.S. Rahman, P.A. Dowben, Adsorbate doping of MoS_2 and WSe_2: the influence of Na and Co, J. Phys. Condens. Matter 29 (2017), 285501, https://doi.org/10.1088/1361-648X/aa7482.

[59] G. Plechinger, A. Castellanos-Gomez, M. Buscema, H.S.J. van der Zant, G.A. Steele, A. Kuc, T. Heine, C. Schüller, T. Korn, Control of biaxial strain in single-layer molybdenite using local thermal expansion of the substrate, 2D Mater. 2 (1) (2015) 015006, https://doi.org/10.1088/2053-1583/2/1/015006.